Advances in Condensed Matter Physics

Surface and Interface Sciences in Microfluidic Systems

Lead Guest Editor: Xiang-Dong Liu
Guest Editors: Sang Woo Shin and Cheng Yu

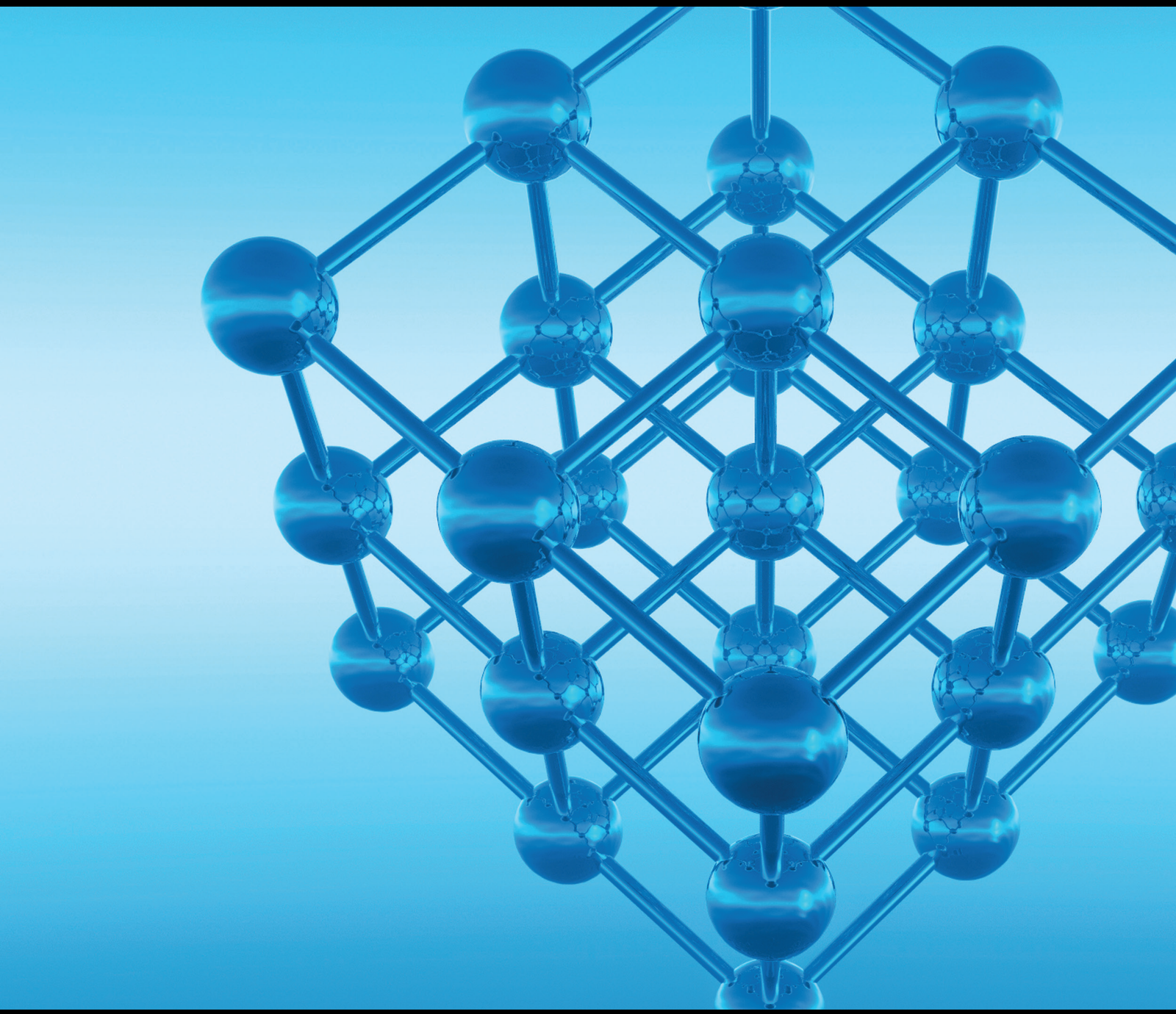

Surface and Interface Sciences in Microfluidic Systems

Advances in Condensed Matter Physics

Surface and Interface Sciences in Microfluidic Systems

Lead Guest Editor: Xiang-Dong Liu
Guest Editors: Sang Woo Shin and Cheng Yu

Contents

Hindawi
Advances in Condensed Matter Physics
Volume 2019, Article ID 1974952, 9 pages
https://doi.org/10.1155/2019/1974952

Research Article

Experimental Study on Liquid Flow and Heat Transfer in Rough Microchannels

Xuan Zhang,[1] Taocheng Zhao,[1] Suchen Wu,[1] and Feng Yao[2]

[1]*Key Laboratory of Energy Thermal Conversion and Control of Ministry of Education, School of Energy and Environment, Southeast University, Nanjing 210096, China*
[2]*Jiangsu Key Laboratory of Micro and Nano Heat Fluid Flow Technology and Energy Application, School of Environmental Science and Engineering, Suzhou University of Science and Technology, Suzhou, Jiangsu 215009, China*

Correspondence should be addressed to Suchen Wu; scwu2010@seu.edu.cn

Received 30 July 2019; Revised 21 October 2019; Accepted 30 October 2019; Published 23 November 2019

Guest Editor: Sang Woo Shin

Although roughness is negligible for laminar flow through tubes in classic fluid mechanics, the surface roughness may play an important role in microscale fluid flow due to the large ratio of surface area to volume. To further verify the influence of rough surfaces on microscale liquid flow and heat transfer, a performance test system of heat transfer and liquid flow was designed and built, and a series of experimental examinations are conducted, in which the microchannel material is stainless steel and the working medium is methanol. The results indicate that the surface roughness plays a significant role in the process of laminar flow and heat transfer in microchannels. In microchannels with roughness characteristics, the Poiseuille number of liquid laminar flow relies not only on the cross section shape of the rough microchannels but also on the Reynolds number of liquid flow. The Poiseuille number of liquid laminar flow in rough microchannels increases with increasing Reynolds number. In addition, the Nusselt number of liquid laminar heat transfer is related not only to the cross section shape of a rough microchannel but also to the Reynolds number of liquid flow, and the Nusselt number increases with increasing Reynolds number.

1. Introduction

Microscale heat transfer and fluid flow are widely present in micro-electromechanical systems [1], chip laboratories [2, 3], biomedical testing [4], microelectronic chip cooling [5], fuel cells [6], microreactors, and other frontier scientific and technological fields [7, 8]. The research in this field is of great importance at the scientific level for exploring the law of microscale heat and mass transfer. With the rapid development of microfluidic devices, the size of the channel is becoming increasingly smaller, and the ratio of the surface area to the volume of the channel is increasing sharply. As a result, the effect exerted on heat transfer and fluid flow in microchannels by surface roughness is becoming increasingly prominent [9, 10], and the influence mechanism has attracted attention around the world [9, 11]. At present, the role of rough surfaces in microscale heat transfer and flow has not been fully revealed.

The MEMS microchannel heat sink was initially proposed by Tuckerman and Pease [12] in the early 1980s. It possesses the advantages of small size, more area for heat transfer in a limited volume, which contributes to a comparably large heat transfer coefficient. Using microchannel heat sinks has become an important way to deal with the issue of heat dissipation from electronic chips. The microchannel is usually defined as the channel with a size of $10\,\mu\text{m} \le D_h \le 200\,\mu\text{m}$, in which D_h is the equivalent diameter of the channel [13]. In recent years, scholars in various countries have carried out many theoretical studies on heat transfer and fluid flow in microchannels. Li et al. [14] studied the characteristics of laminar flow and heat transfer in trapezoidal and triangular silicon microchannels in a numerical way and made a comparison with the experimental results. The effect of Reynolds number on Nusselt number was discussed from the view of the field synergy principle. Chen and Zhang et al. quantitatively defined the roughness

structures in microchannels with the fractal theory, which is further expanded by Deng et al. to the construction of porous metal foams [15], and carried out a series of numerical investigations on the effect of relative roughness, the fractal dimension on the heat transfer [16, 17]. Cole and Çetin [18] solved a coupled heat transfer process in parallel-plate microchannels under constant heat flow conditions by means of Green's functions and then obtained analytical solutions in integral form and studied the effect of wall axial heat conduction on liquid flow and heat transfer in microchannels. They also analyzed the influence of flow velocity, length of the heating section, wall thickness, and wall heat coefficient on the average and local Nusselt numbers.

Though the fruitful achievements were obtained based on the theoretical analysis, there have been relatively few reports on experimental results. Kandlikar et al. [19] found that, under the same average roughness conditions, a change in the serrated arrangement of serrated rough surfaces leads to a change in the characteristics of laminar flow in microchannels. This means that the average roughness is not enough to fully reflect the characteristics of rough surfaces, and it is difficult to rely solely on the single index of average roughness to fully explain the influence of roughness on flow characteristics. Kandlikar et al. [20] also measured the effect of surface roughness of stainless-steel small passages with inner diameters of 1.032 mm and 0.62 mm (obtained from acid etching) on the characteristics of flow heat transfer and pressure drop. It was found that the roughness enhanced heat transfer and led to a significant increase in pressure drop. Shen et al. experimentally investigated the single-phase convective heat transfer in a compact heat sink with rectangular microchannels and found that the Reynolds number has a significant effect on the heat transfer capability [21].

In classic fluid mechanics, roughness is nearly negligible for fluid flow in tubes. When the channel size is in microscale, the influence of roughness may permeate into the main flow in the microchannel. In this context, it is expected that the roughness on the surface may play a vital role in microscale fluid flow. To further verify the influence of rough surfaces on microscale liquid flow and heat transfer, the three-dimensional morphology of a stainless-steel surface was observed by scanning electron microscopy, and a performance test system for heat transfer and liquid flow in rough microchannels was designed and built. The variations in the Poiseuille number of liquid laminar flow and Nusselt number of liquid laminar convection heat transfer in rough microchannels with Reynolds number were obtained in this paper.

2. Experimental Description

2.1. Experimental System. The experimental principles of the liquid flow performance measurement in rough microchannels are presented in Figure 1. Methanol was used as the working fluid in the experiments. Driven by injection pumps, the working fluid in syringes flowed through a regulating valve, a constant temperature fluid circulator, a filter, and the experimental section sequentially and finally flowed into glassware (beaker) placed on an electronic balance. The flow rate of the liquid entering the microchannel was precisely controlled by adjusting the velocity of the liquid pushed by the injection pump, and different flow pressure drop was further obtained. Moreover, the temperature of the liquid entering the microchannel was adjusted by a constant-temperature fluid circulator. The temperature of the liquid inlet in the microchannel was measured by a thermocouple, the pressure drop of the liquid flow in the microchannel was measured by a differential pressure sensor, and the flow rate of the liquid could be set by injection pumps. When the flow rate changed, the flow pressure drop in the microchannel also changed accordingly, which could be obtained by a data acquisition instrument through the differential pressure sensor.

Figure 1 shows that the experimental system for measuring liquid flow performance in rough microchannels is composed of liquid flow control and pressure driving device, experimental section, flow pressure drop testing device, and data acquisition device. The components used in the microscale liquid flow experiments are described in detail as follows.

The liquid flow control and pressure-driving device consists of injection pumps, syringes, and connecting pipes. Two injection pumps with the same size are used in parallel during the experiments, and each of them is equipped with a regulating valve. When one injection pump works, the other injection pump can extract additional working fluid into its syringe over time. Therefore, the continuity and stability of the liquid flow condition can be achieved by switching the injection pumps over time. High-pressure injection pumps are used in the experiments due to the large flow resistance in the microchannels. The inner diameter of the stainless steel syringe is 28.6 mm, and the capacity is 50 mL (see Table 1 for specifications and main parameters), thus ensuring sufficient fluid transport capacity.

The experimental section is mainly composed of rough microchannels and connecting pipes. The rough microchannels are made of stainless steel circular microchannels (Figure 2), which are divided into two types: the inner diameter is 152 μm and 206 μm and the outer diameter is 300 μm and 450 μm, respectively. The average surface roughness heights corresponding to the stainless steel microchannels with inner diameters of 152 μm and 206 μm are 6.65 μm and 6.14 μm, respectively. Channel roughness is generated naturally during microtubule processing. Scanning electron microscopy (SEM) images of the cross sections of the channels and the roughness of the inner surfaces are presented in Figure 3, and the measurements are completed by field emission scanning electron microscopy.

The flow pressure drop test device is composed of a differential pressure sensor and a connecting pipe. Since the range of the pressure drop of the fluid flow in microchannels varies greatly under different working conditions in these experiments, two differential pressure sensors with pressure ranges of 0–200 kPa and 0–500 kPa were selected in the experiments (see Table 1 for specifications and main parameters and Figure 4 for physical photos) to guarantee measurement accuracy, respectively. The connection mode between the differential pressure sensor and microchannel is shown in Figure 5.

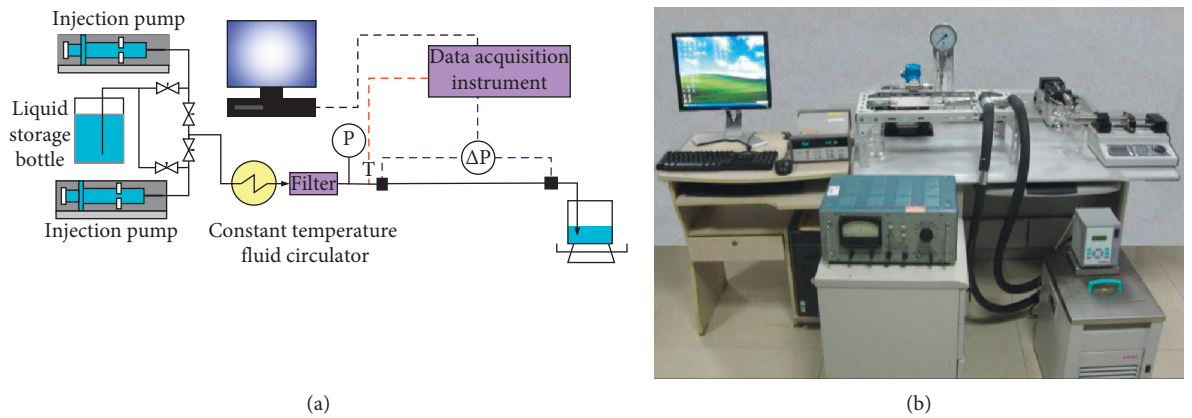

(a) (b)

Figure 1: An experimental system for measuring liquid flow properties in microchannels: (a) schematic diagram and (b) physical photograph.

Table 1: Main experimental instruments and equipment and their parameters.

Serial number	Name of instrument and equipment	Specification type, equipment manufacturer, main parameters
1	Single-channel high-pressure injection pump	Model: LSP01-1BH, Baoding Langer Constant Current Pump Co., Ltd. Flow range: 192.7 mL/h~5010.9 mL/h. Flow pushing accuracy: +0.5%. Push pressure: greater than 0.56 MPa
2	Differential pressure sensor	Model: CYR-3D, Shanghai Lingsheng Electronic Instrument co., Ltd. Measurement accuracy: 0.3%, range: 200 kPa and 500 kPa
3	Data acquisition instrument	Model: 34970A, AGILENT Company Scanning rate: 250 channels/s, 3 slots
4	Filter	Model: SS-4F-2, SWAGELOK, USA Size of filter core hole: 0.5 um
5	Thermocouple	Type K, OMEGA Engineering Company, USA The diameter of the thermoelectrode is 0.1 mm.
6	Electric heating rod	Customized
7	Constant temperature fluid circulator	Model: MC, German JULABO company Temperature control range: −35~200 adjustable
8	Voltage regulating transformer	Model: TDGC, 0–250 V adjustable
9	DC regulated power supply	Model: WYJ-45A, Tianjin Radio Component Factory 3 Voltage regulation range: 0~45 V adjustable
10	Field emission scanning electron microscope	Model: ultra plus, ZEISS Germany Resolution: 1 nm @ 15 kV; acceleration voltage: 0.02 kV to 30 kV

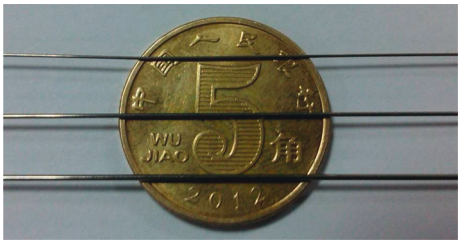

Figure 2: Stainless steel circular microchannels.

The data acquisition device is composed of a data acquisition instrument, data acquisition module, and computer. The signal lines of a temperature sensor and pressure sensor are connected to the data acquisition module, which is inserted into the module slot of the data acquisition device. An Agilent 34970A data acquisition instrument and Agilent 34901A data acquisition module produced by Agilent Company were used in the experiments. The data acquisition instrument is equipped with Agilent Benchlink Data Logger

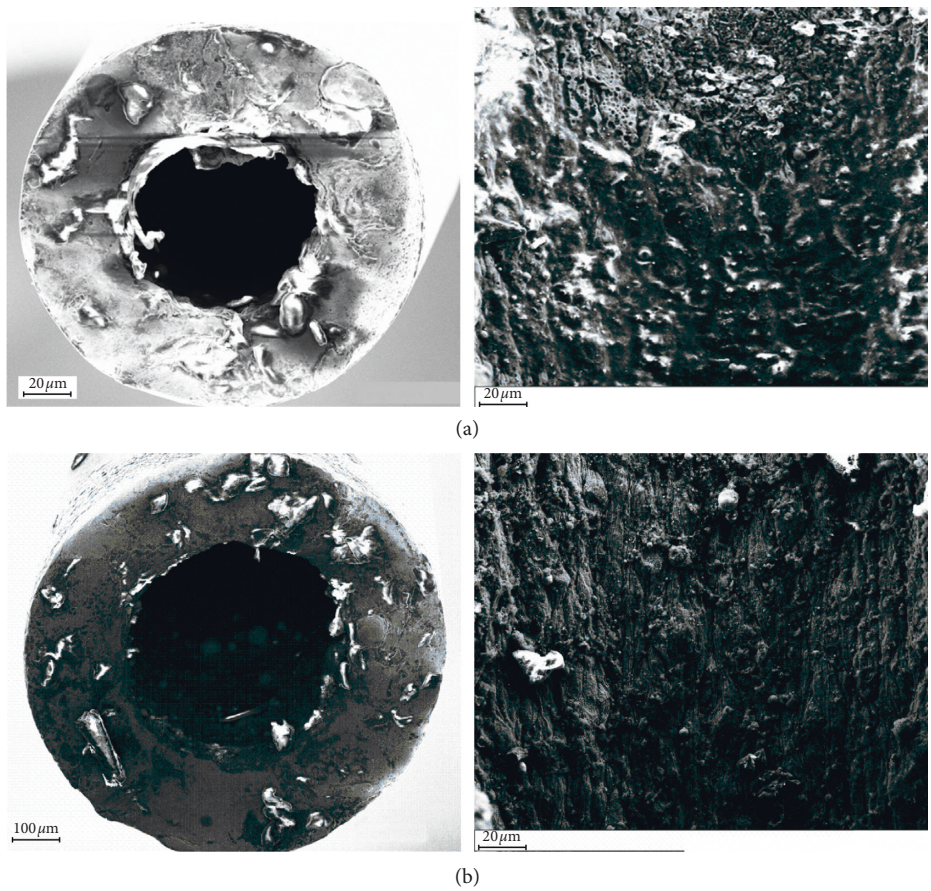

Figure 3: Physical images of the cross sections and rough surfaces of microchannels: (a) $d = 152\,\mu$m; (b) $d = 206\,\mu$m.

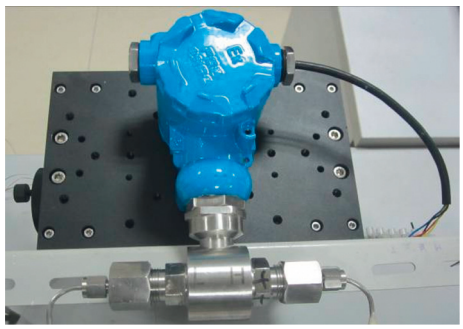

Figure 4: Differential pressure sensor (type: CYR-3D).

data acquisition software, which can record, collect, display, and save the measured data in real time on the computer.

On the basis of the abovementioned experimental platform for liquid flow in rough microchannels (Figure 1), experimental research on the liquid convection heat transfer characteristics in rough microchannels can be carried out by just adding a heat source to the experimental section and assisting the measurement of wall temperature of microchannel heat exchanger tubes. Figure 6 shows the experimental section in the experiment of examining the convection heat transfer, which consists of an upper cover plate, a microchannel heat exchanger tube, a heat-conducting block, an electric heating rod, and a lower cover plate. The upper cover plate, the heat-conducting block, and the lower cover plate are all made of aluminum plates by a milling machine. A rough microchannel of the stainless steel tube with the same specifications as in the microflow experiments is adopted in the microchannel heat exchanger tube.

The electric heating rod is used to simulate the heating element, and the heat generated by it is transferred to the microchannel heat exchanger via the heat-conducting block. The heat in the microchannel heat exchanger is carried away by the convective heat transfer of the working fluid methanol. The thermal insulation material is wrapped on the outer surface of the experimental section to realize the thermal insulation of the experimental section. According to the principle of heat balance, the heat carried by the liquid working medium is transferred to the microchannel heat exchanger by the electric rod. The wall temperature along the microchannel is measured by a thermocouple. Five thermocouples are arranged on the wall of the rough microchannel heat exchanger tube, and the thermocouple wires are drawn to the data acquisition instrument through small round holes in the upper cover plate.

The electric heating rod is connected to a DC-regulated power supply, and the heating power generated by the heating rod is controlled by changing the DC-regulated power supply to regulate the heating flux on the surface of

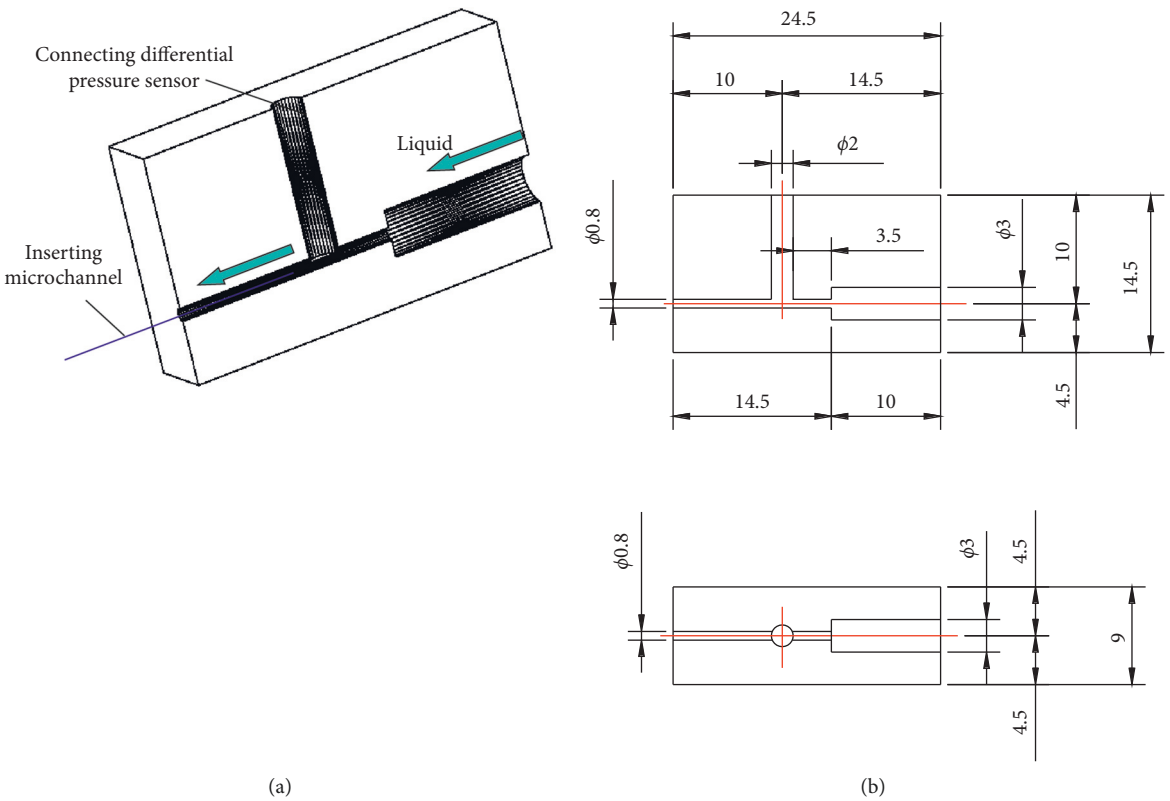

Figure 5: Connection between the differential pressure sensor and microchannel: (a) schematic diagram; (b) size of the connection structure (unit: mm).

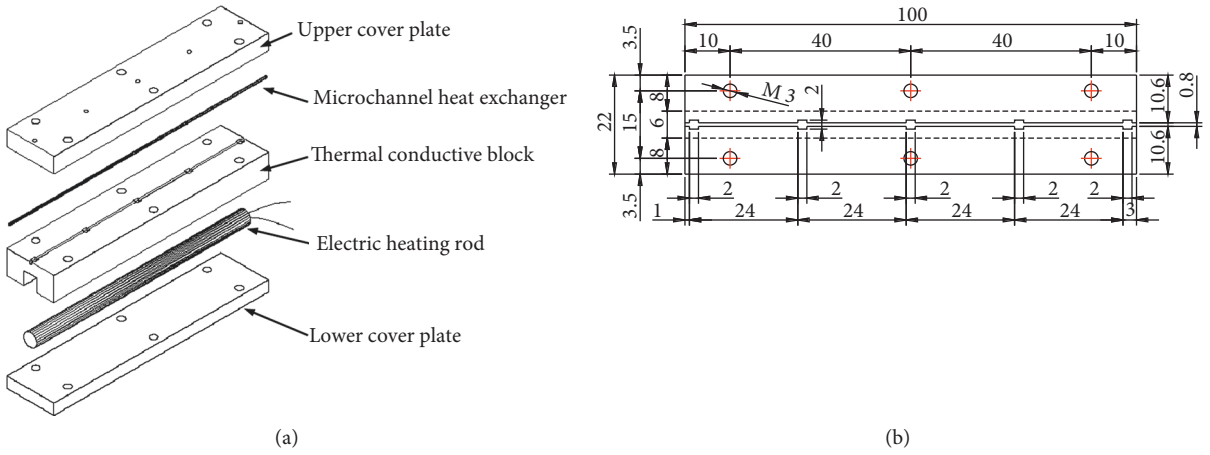

Figure 6: Schematic diagram of the heat transfer and liquid flow test sections in a microchannel: (a) schematic diagram; (b) structure size of heat-conducting block.

the microchannel. By setting the flow rate of the injection pump to adjust the flow rate of liquid in the microchannel, the experimental conditions of heat transfer and flow in the microchannel under different Reynolds numbers were obtained, and the temperature of the liquid entering the microchannels was adjusted by a constant-temperature fluid circulator.

2.2. Experimental Data and Error Analysis

2.2.1. Fluid Flow. The Poiseuille number (Po = fRe) is used to evaluate the flow resistance characteristics of the working fluid in microchannels with roughness in this paper, and the flow frictional resistance coefficient f is defined as follows [22]:

$$f = \Delta P \cdot \frac{d}{L} \cdot \frac{1}{2\rho_l \overline{u}_l{}^2}, \tag{1}$$

where ΔP is the on-way resistance of liquid flow in rough microchannels, d represents the diameter of circular microchannels, L symbolizes the length of channels, and ρ_l is the density of the liquid. The average velocity of the liquid flowing through the cross section of the microchannel $\overline{u}_l$ is

$$\overline{u}_l = \frac{G_l}{A} = \frac{4G_l}{\pi d^2}, \tag{2}$$

where G_l is the volume flow rate of liquid and A is the cross-sectional area of the channel. The Reynolds number of liquid methanol flowing in microchannels can be expressed as follows:

$$\mathrm{Re} = \frac{\overline{u}_l d \rho_l}{\mu_l} = \frac{4G_l \rho_l}{\pi\, d \mu_l}, \tag{3}$$

where the dynamic viscosity of the liquid is μ_l. The Poiseuille number of liquid flowing in the microchannel can be obtained by simultaneously solving equations (1) and (3) as follows:

$$\mathrm{Po} = f\mathrm{Re} = \frac{2\pi \Delta P d^4}{L G_l \mu_l}. \tag{4}$$

2.2.2. Heat Transfer. The average convective heat transfer coefficient of methanol flowing in stainless steel microchannels with inner diameter d and length L is

$$\overline{h} = \frac{Q}{A\left(\overline{T}_w - \overline{T}_l\right)}, \tag{5}$$

where the heat Q transferred from the heat source to the working fluid through the wall of the microchannel is the heat carried away by the working fluid, i.e.,

$$Q = G_l \rho_l C_{p,l}\left(T_{\mathrm{out},l} - T_{\mathrm{in},l}\right). \tag{6}$$

The total heat transfer area of the microchannel heat exchanger tube is

$$A = \pi \mathrm{d} L, \tag{7}$$

and the average temperature of the liquid working fluid is

$$\overline{T}_l = \frac{T_{\mathrm{in},l} + T_{\mathrm{out},l}}{2}. \tag{8}$$

The average wall temperature of the channel is

$$\overline{T}_w = \frac{T_{w,1} + T_{w,2} + T_{w,3} + T_{w,4} + T_{w,5}}{5}. \tag{9}$$

The average Nusselt number of heat transfer and liquid flow in the microchannel can be obtained by simultaneously solving equations (5)~(9) as

$$\begin{aligned}\overline{\mathrm{Nu}} &= \frac{\overline{h} d}{\lambda_l} = \frac{Q}{A\left(\overline{T}_w - \overline{T}_l\right)} \frac{d}{\lambda_l} \\ &= \frac{G_l \rho_l C_{p,l}\left(T_{\mathrm{out},l} - T_{\mathrm{in},l}\right)}{\pi \lambda_l L\left(\left(T_{w,1} + T_{w,2} + T_{w,3} + T_{w,4} + T_{w,5}/5\right) - \left(T_{\mathrm{in},l} + T_{\mathrm{out},l}/2\right)\right)},\end{aligned} \tag{10}$$

where $C_{p,l}$ is the specific heat capacity of the liquid; $T_{\mathrm{out},l}$ and $T_{\mathrm{in},l}$ are the inlet and outlet temperatures of the liquid in the microchannel, respectively. $T_{w,1}$, $T_{w,2}$, $T_{w,3}$, $T_{w,4}$, and $T_{w,5}$ are the measured surface temperatures along the wall of the microchannel; G_l is the volume flow of liquid through the heat exchanger tubes; and λ_1 is the thermal conductivity of the liquid. It should be pointed out that the average temperature of the liquid at the inlet and outlet is taken as the qualitative temperature for the physical parameters of the liquid involved in the above formula.

2.3. Error Analysis. The indirectly measured y and multiple independent directly measured $x_1, x_2, \ldots$, have the following functional relationship,

$$y = f\left(x_1, x_2, x_3, \ldots, x_n\right). \tag{11}$$

The standard errors of x_1, x_2, …, are δx_1, δx_2, …, respectively, and then the standard errors of y can be obtained by the following formula [23]:

$$\delta y = \sqrt{\left(\frac{\partial f}{\partial x_1}\delta x_1\right)^2 + \left(\frac{\partial f}{\partial x_2}\delta x_2\right)^2 + \cdots + \left(\frac{\partial f}{\partial x_n}\delta x_n\right)^2}, \tag{12}$$

where the error transfer coefficient is $\partial f / \partial x$. According to formulas (4), (10), and (12), the uncertainty of the Poiseuille number and Nusselt number can be deduced as follows, respectively:

$$\begin{aligned}\frac{\delta \mathrm{Po}}{\mathrm{Po}} &= \pm\left[\left(4\frac{\delta d}{d}\right)^2 + \left(\frac{\delta G_l}{G_l}\right)^2 + \left(\frac{\delta \mu_l}{\mu_l}\right)^2 + \left(\frac{\delta \Delta P/L}{\Delta P/L}\right)^2\right]^{1/2}, \\ \frac{\delta \overline{\mathrm{Nu}}}{\overline{\mathrm{Nu}}} &= \pm\left[\left(\frac{\delta Q/A}{Q/A}\right)^2 + \left(\frac{\delta d}{d}\right)^2 + \left(\frac{\delta \lambda_l}{\lambda_l}\right)^2 + \left(\frac{\delta\left(\overline{T}_w - \overline{T}_l\right)}{\overline{T}_w - \overline{T}_l}\right)^2\right]^{1/2}.\end{aligned} \tag{13}$$

The measurement errors of the main parameters involved in these experiments are listed in Table 2.

Before conducting the fluid flow and heat transfer experiments on such a performance test system, a validation examination on this system with a conventional circular channel was launched, in which the diameter of the channels is 3 mm. The pressure drop and the temperature distribution of the liquid laminar flow in this smooth channel are experimentally examined. The Poiseuille number and Nusselt number in the experiment are evaluated as 16.7 and 4.3 when Reynolds number is $1000 < \mathrm{Re} < 2000$, which are consistent with the classic values of Po = 16.0, Nu = 4.36 for

Table 2: List of experimental errors.

Parameter	Uncertainty	Parameter	Uncertainty
G_l	0.5%	λ_l	0.02%
ρ_l	0.07%	μ_l	0.6%
L	1.4%	$\overline{T}_w - \overline{T}_l$	2.5%
d	1.7%	Q/A	2.4%
ΔP	0.3%	$\Delta P/L$	1.5%
Po	7.0%	$\overline{\mathrm{Nu}}$	3.9%

liquid laminar flow in conventional circular channels, verifying the validity of this experimental approach [24, 25].

3. Results and Discussion

3.1. Fluid Flow in Rough Microchannels. Based on the experimental system shown in Figure 1, the flow pressure drop in rough stainless microchannels with diameters of 152 μm and 206 μm and length of 7.2 cm was examined. Figure 7 demonstrates the variation of pressure drop with volume flow, and it is observed that the flow pressure drop increases with increasing liquid flow rate. Under the condition of the same flow rate, a decrease in channel diameter leads to rapid growth in the flow pressure drop along the microchannel. The flow pressure drop along the 152 μm microchannel is approximately 3.5 times that of the 206 μm microchannel.

The variation in the Poiseuille number of liquid flow in microchannels with Reynolds numbers measured by experiments is displayed in Figure 8. Note that the dash-dot line in the figure is the classic value of Poiseuille number for liquid laminar flow in conventional size channels. Generally, for fluid flow in conventional channels, Poiseuille number is just dependent on the shape of the cross section of the channel according to the theory of classical fluid mechanics [24, 25]. However, it is seen in Figure 8 that the Poiseuille number of liquid laminar flow in rough microchannels relies not only on the shape of the cross section of the channel but also on the Reynolds number of the liquid flow. With an increase in the Reynolds number, the roughness results in an increase in the Poiseuille number of liquid laminar flow in the microchannels, indicating that the laminar flow characteristics in rough microchannels differ from those in conventional microchannels.

In roughness microchannels, the uneven surface distribution disturbs the laminar flow near the wall surface and even contributes to the occurrence of eddies in the concave of these rough structures. Since the size of the rough structure (~1 mm) is comparable to the diameter of the roughness microchannel (~100 mm), these induced eddies would inevitably result in the increase of on-way flow resistance. As a result, the Poiseuille number of the laminar flow in roughness microchannels gets elevated when compared with that obtained in conventional channels. Besides, the effect of eddies on the mainstream flow becomes more significant with the increase of Reynolds number, and thus the Poiseuille number gets more deviated from the classic value.

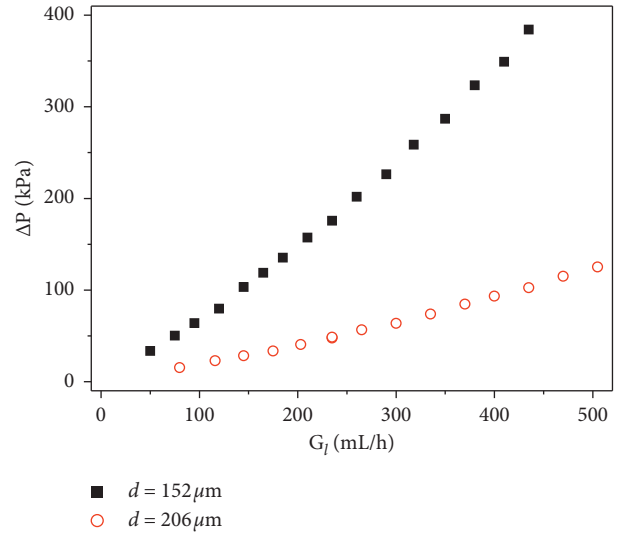

Figure 7: Pressure drop of liquid flow in microchannels at different flow rates (T = 40°C, L = 7.2 cm).

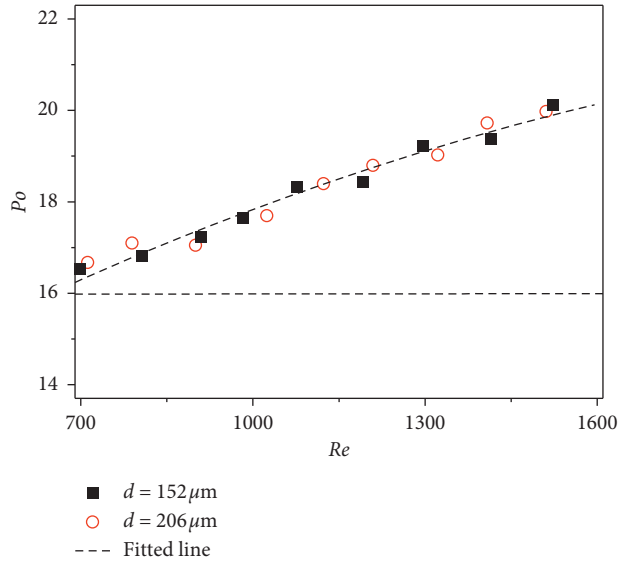

Figure 8: Influence of the Reynolds number on the Poiseuille number of liquid flow in microchannels.

In addition, to clearly reveal the relationship of Reynolds number and Poiseuille number in the circular roughness microchannel, following the work of Wu and Cheng [26], a correlation equation with the consideration of the relative roughness is proposed as $\mathrm{Po} = C_1 \varepsilon^{a_1} \mathrm{Re}^{b_1}$, in which ε is the relative surface roughness of the microchannel. Based on the obtained experimental data, the parameters in the equation are fitted as $C_1 = 3.04$, $a_1 = -0.001$, and $b_1 = 0.256$. The correlation equation is also plotted in Figure 8, and it is seen that it well predicts the relationship between Poiseuille number and Reynolds number.

3.2. Heat Transfer in Rough Microchannels. The variation in the wall temperature along the flow direction of the

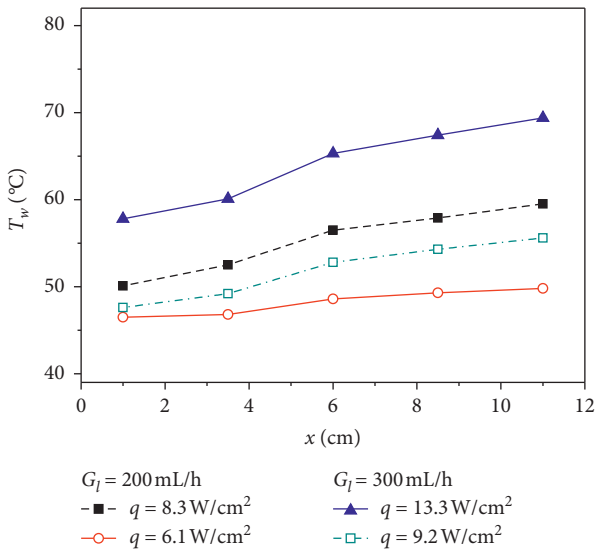

Figure 9: Wall temperature of microchannels (liquid inlet temperature of 25°C).

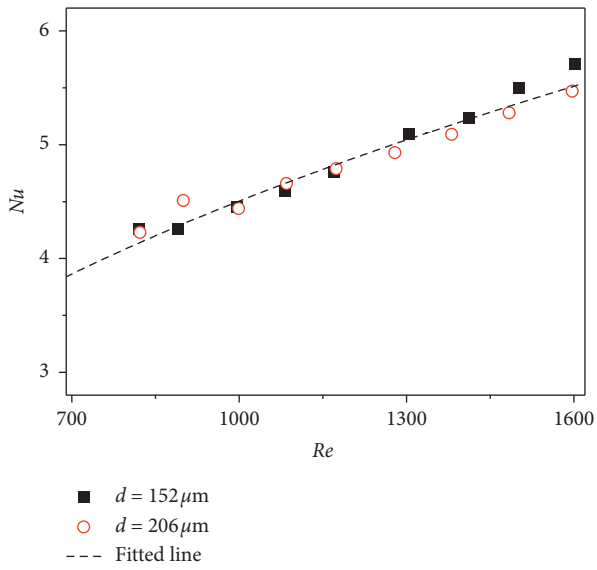

Figure 10: Effect of the Reynolds number on the Nusselt number.

microchannel with a diameter of 152 μm under different flow and heat loads is depicted in Figure 9. The distribution of temperature on the wall of the microchannel is determined by the heat load and fluid flow rate, and the graph shows that the wall temperature increases approximately linearly along the wall. It is also seen that the wall temperature increases with the increase of heat flux at the same liquid inlet flow rate.

The change in the Nusselt number of liquid convection heat transfer in rough stainless microchannels with diameters of 152 μm and 206 μm with the Reynolds number is listed in Figure 10. The figure shows that the Nusselt number of laminar flow and heat transfer in rough microchannels is not only dependent on the shape of the cross section but also on the Reynolds number of liquid flow. It is observed in the figure that the Nusselt number of liquid laminar convection heat transfer increases with increasing Reynolds number.

It is believed that the peaks of rough structures in microchannel reduce the flow area of the microchannel, resulting in an increase of the local velocity. Consequently, the local Nusselt number of the laminar flow heat transfer gets improved. More importantly, the convex and concave structures on the channel wall disturb the regular distribution of the thermal boundary layer. Together with the induced eddies near the microchannel wall surface, both then contribute to the increase of the local Nusselt number.

Similarly, a correlation equation of Nusselt number and Reynolds number is proposed for the prediction of laminar flow heat transfer in the circular roughness microchannel, and it is expressed as $\mathrm{Nu} = C_2 \varepsilon^{a_2} \mathrm{Re}^{b_2}$. The obtained correlation equation, with fitted parameters of $C_2 = 0.24$, $a_2 = 0.012$, and $b_2 = 0.431$, is also illustrated in Figure 10, presenting the acceptable agreement with experimental data.

4. Conclusions

In this study, a performance test system of heat transfer and liquid flow in rough microchannels was designed and built, and an experimental examination of heat transfer and liquid flow in rough microchannels was carried out, in which the three-dimensional morphology of the rough surface was observed by scanning electron microscopy. The Poiseuille number of liquid laminar flow and the Nusselt number of liquid laminar convection heat transfer in rough microchannels were obtained as a function of the Reynolds number. The major conclusions are drawn as follows:

(1) In rough microchannels, the Poiseuille number of liquid laminar flow relies not only on the shape of the cross section of the channel but also on the Reynolds number of liquid flow. The Poiseuille number of liquid laminar flow in rough microchannels increases with increasing Reynolds number, and the influence of roughness on liquid flow in rough microchannels gets much more obvious with the increase of the Reynolds number.

(2) In rough microchannels, the Nusselt number of liquid laminar flow heat transfer is related not only to the shape of the cross section of the channel but also to the Reynolds number of liquid flow, i.e., the Nusselt number raises with the increase of the Reynolds number.

Data Availability

The data used to support the findings of this study are available from the corresponding author upon request.

Conflicts of Interest

The authors declare that there are no conflicts of interest regarding the publication of this article.

Acknowledgments

The authors are grateful for the guidance from Dr. Chengbin Zhang at Southeast University. This work was supported by the National Natural Science Foundation of China (grant nos. 51906170 and 51776037).

References

[1] C.-M. Ho and Y.-C. Tai, "Micro-electro-mechanical-systems (MEMS) and fluid flows," *Annual Review of Fluid Mechanics*, vol. 30, no. 1, pp. 579–612, 1998.

[2] Y. Chen, W. Gao, C. Zhang, and Y. Zhao, "Three-dimensional splitting microfluidics," *Lab on a Chip*, vol. 16, no. 8, pp. 1332–1339, 2016.

[3] Z. Liu, M. Li, Y. Pang, L. Zhang, Y. Ren, and J. Wang, "Flow characteristics inside droplets moving in a curved microchannel with rectangular section," *Physics of Fluids*, vol. 31, no. 2, Article ID 022004, 2019.

[4] S. R. Yadhuraj, S. Babu Gandla, S. S. Omprakash, B. G. Sudarshan, and S. C. Prasanna Kumar, "Design and development of micro-channel using PDMS for biomedical applications," *Materials Today: Proceedings*, vol. 5, no. 10, pp. 21392–21397, 2018.

[5] C. Zhang, Y. Chen, R. Wu, and M. Shi, "Flow boiling in constructal tree-shaped minichannel network," *International Journal of Heat and Mass Transfer*, vol. 54, no. 1–3, pp. 202–209, 2011.

[6] N. Ibrahim-Rassoul, E.-K. Si-Ahmed, A. Serir, A. Kessi, J. Legrand, and N. Djilali, "Investigation of two-phase flow in a hydrophobic fuel-cell micro-channel," *Energies*, vol. 12, no. 11, pp. 2061, 2019.

[7] C. Zhang, F. Yu, X. Li, and Y. Chen, "Gravity-capillary evaporation regimes in microgrooves," *AIChE Journal*, vol. 65, no. 3, pp. 1119–1125, 2019.

[8] J. Wang, W. Gao, H. Zhang, M. Zou, Y. Chen, and Y. Zhao, "Programmable wettability on photocontrolled graphene film," *Science Advances*, vol. 4, no. 9, Article ID eaat7392, 2018.

[9] J. B. Taylor, A. L. Carrano, and S. G. Kandlikar, "Characterization of the effect of surface roughness and texture on fluid flow-past, present, and future," *International Journal of Thermal Sciences*, vol. 45, no. 10, pp. 962–968, 2006.

[10] C. Zhang, Z. Deng, and Y. Chen, "Temperature jump at rough gas-solid interface in couette flow with a rough surface described by Cantor fractal," *International Journal of Heat and Mass Transfer*, vol. 70, pp. 322–329, 2014.

[11] X. Liu, Y. Chen, and M. Shi, "Dynamic performance analysis on start-up of closed-loop pulsating heat pipes (CLPHPs)," *International Journal of Thermal Sciences*, vol. 65, pp. 224–233, 2013.

[12] D. B. Tuckerman and R. F. W. Pease, "High-performance heat sinking for VLSI," *IEEE Electron Device Letters*, vol. 2, no. 5, pp. 126–129, 1981.

[13] S. Kandlikar, "Heat transfer, pressure drop and flow patterns during flow boiling in parallel channel compact heat exchangers of small hydraulic diameters," *Heat Transfer Engineering*, vol. 23, no. 5, pp. 5–23, 2001.

[14] Z. Li, W.-Q. Tao, and Y.-L. He, "A numerical study of laminar convective heat transfer in microchannel with non-circular cross-section," in *Proceedings of the ASME 3rd International Conference on Microchannels and Minichannels*, pp. 351–360, American Society of Mechanical Engineers (ASME), Toronto, Canada, June 2005.

[15] Z. Deng, X. Liu, C. Zhang, Y. Huang, and Y. Chen, "Melting behaviors of PCM in porous metal foam characterized by fractal geometry," *International Journal of Heat and Mass Transfer*, vol. 113, pp. 1031–1042, 2017.

[16] C. Zhang, Y. Chen, M. Shi, Y. Huang, and Y. Chen, "Effects of roughness elements on laminar flow and heat transfer in microchannels," *Chemical Engineering and Processing: Process Intensification*, vol. 49, no. 11, pp. 1188–1192, 2010.

[17] Y. Chen, C. Zhang, M. Shi, and Y. Yang, "Thermal and hydrodynamic characteristics of constructal tree-shaped minichannel heat sink," *AIChE Journal*, vol. 56, no. 8, pp. 2018–2029, 2010.

[18] K. D. Cole and B. Çetin, "The effect of axial conduction on heat transfer in a liquid microchannel flow," *International Journal of Heat and Mass Transfer*, vol. 54, no. 11-12, pp. 2542–2549, 2011.

[19] S. G. Kandlikar, D. Schmitt, A. L. Carrano, and J. B. Taylor, "Characterization of surface roughness effects on pressure drop in single-phase flow in minichannels," *Physics of Fluids*, vol. 17, no. 10, p. 100606, 2005.

[20] S. G. Kandlikar, S. Joshi, and S. Tian, "Effect of surface roughness on heat transfer and fluid flow characteristics at low reynolds numbers in small diameter tubes," *Heat Transfer Engineering*, vol. 24, no. 3, pp. 4–16, 2003.

[21] S. Shen, J. Xu, J. Zhou, and Y. Chen, "Flow and heat transfer in microchannels with rough wall surface," *Energy Conversion and Management*, vol. 47, no. 11-12, pp. 1311–1325, 2006.

[22] R. Shah and A. London, "Laminar flow forced convection in ducts," in *Advances in Heat Transfer*, Academic Press, New York, NY, USA, 1978.

[23] J. Stoer and R. Bulirsch, *Introduction to Numerical Analysis*, Springer Science & Business Media, Berlin, Germany, 2013.

[24] J. P. Holman, *Heat Transfer*, McGraw-Hill Education, New York, NY, USA, 10th edition, 2010.

[25] F. M. White, *Fluid Mechanics*, McGraw-Hill Education, New York, NY, USA, 8th ed edition, 2016.

[26] H. Y. Wu and P. Cheng, "An experimental study of convective heat transfer in silicon microchannels with different surface conditions," *International Journal of Heat and Mass Transfer*, vol. 46, no. 14, pp. 2547–2556, 2003.

Hindawi
Advances in Condensed Matter Physics
Volume 2019, Article ID 5726974, 11 pages
https://doi.org/10.1155/2019/5726974

Research Article

Hydrodynamics of Compound Droplet Flowing in the Curved Minichannel

Meimei Sun,[1] Miao Zhao,[1] and Wei Gao[1,2]

[1]*Key Laboratory of Energy Thermal Conversion and Control of Ministry of Education, School of Energy and Environment, Southeast University, Nanjing 210096, China*
[2]*School of Engineering and Applied Science, Harvard University, Cambridge 02138, USA*

Correspondence should be addressed to Wei Gao; weigao@seu.edu.cn

Received 3 August 2019; Revised 24 September 2019; Accepted 1 October 2019; Published 15 October 2019

Guest Editor: Xiang-Dong Liu

Based on the volume of fluid (VOF) method, a theoretical model of compound droplet deformation in curved minichannel is developed. The effects of curved angle, continuous phase, radius ratio between the inner and integral droplets, and viscosity of the middle phase are examined to reveal the underlying mechanism of compound droplet deformation. The results indicate that the deformation process of the compound droplets in the curved minichannel can be divided into three stages, namely, the initial stage, the turning stage, and the adjustment stage. Both large curved angle and high capillary number of the continuous phase result in the large shear force and high eccentricity of the compound droplet. However, as the radius ratio increases, the influence of the inner droplet on the deformation of the compound droplet transits from enhancing to suppressing.

1. Introduction

Core fluid encapsulated in the shell fluid, referred as compound droplet, is useful in the storage, transportation, and controlled release of the functional materials, which has a great potential in microreactor [1, 2], drug delivery [3, 4], thermal management [5–7], and fusion engineering target [8–10]. Usually, the channel is not designed straightly, so the compound droplet may deform sharply and even break up in the shear flow caused by the curved channel. Therefore, knowing the hydrodynamics of the compound droplets is crucial to precisely control the flow phenomena of the compound droplet paving the way for related applications [11, 12].

Several attempts have been applied to research the multiphase flow phenomena in the curved channel [13, 14]. Che et al. [15, 16] investigate the flow pattern of a confined droplet moving in curved microchannels based on the analytical method. The flow resistance coefficient decreases due to the increasing droplet size and the microchannel curvature. Using the inertial focusing technique, Wewala et al. [17] simulate the cell separation in ascending and descending curvilinear microchannels. Based on the volume of fluid (VOF) method, the hydrodynamics of droplets moving along the serpentine microchannel in the mixing process is studied [18]. However, the available studies are on the hydrodynamics of the single-phase droplet [19]. The compound droplet undergoes a quite different deformation process from the single-phase droplet under the shear force [20]. Chen et al. numerically studied the morphology evolution of the compound droplet under shear [21]. Three kinds of mechanisms are applied to describe the four types of breakup modes. Compared with the single-phase droplet, the compound droplet can exhibit enhancing or suppressing steady deformation, depending on the radius ratio [22]. Nevertheless, the deformation of the compound droplet in a curved channel is still less understood, especially the effect of the flow field on the concentricity and sphericity of the compound droplet.

To provide a guideline for the design of the curved minichannel and the manipulation of the flow field in the curved minichannel, it is extremely important to develop a quantitative analysis that considers the effect of the confinement and the parameters of the liquid. Therefore, based on the VOF method, a theoretical model of the deformation

behaviors of the compound droplets in the curved minichannel is developed to investigate the hydrodynamics of the compound droplets in the curved minichannel. The effects of curved angle, continuous phase, radius ratio, and viscosity of the middle phase are analyzed to reveal the deformation mechanism of the compound droplets in the curved minichannel. The current simulation provides a deep understanding of the hydrodynamic behaviors of the compound droplet in the curved minichannel.

2. Mathematical Model

To investigate the hydrodynamics of the compound droplet in the curved minichannel, a two-dimensional theoretical model of compound droplets flowing in a curved minichannel is developed. As shown in Figure 1(a), the inner diameter of the curved minichannel is $D = 0.5$ mm. The compound droplets flow continuously into the curved minichannel from the left inlet and then through the first straight section with length $L = 6D$. Afterward, the compound droplets turn left at the corner with the turning angle θ and inner curvature radius R and finally flow through the second straight section with the length $H = 4D$. Before the inlet, the compound droplets including middle phase (density ρ_m and viscosity μ_m) and dispersed phase (density ρ_d and viscosity μ_d) are initially set in a rectangular shape and repeat periodically in minichannels, shown in Figure 1(b). The shape of the compound droplets will transform while the droplet is flowing with the continuous phase (density ρ_c and viscosity μ_c).

2.1. Governing Equation. In this study, the VOF method [23–25] is applied to simulate the deformation of the compound droplet in the curved minichannel. The incompressible fluids of the dispersed phase, middle phase, and continuous phase are considered to be Newtonian and immiscible with each other. The volume fraction α in one cell follows the below equation:

$$\alpha_c + \alpha_m + \alpha_d = 1, \tag{1}$$

where α_c, α_m, and α_d are the volume fractions of the continuous phase, middle phase, and dispersed phase, respectively. The density ρ and viscosity μ in one cell are calculated as follows:

$$\begin{aligned} \rho &= \alpha_c\rho_c + \alpha_m\rho_m + \alpha_d\rho_d, \\ \mu &= \alpha_c\mu_c + \alpha_m\mu_m + \alpha_d\mu_d. \end{aligned} \tag{2}$$

The densities of the three phases are all 1000 kg/m^3, so the gravity force is neglected. Moreover, the viscosities of the three phases are $\mu_c = \mu_d = 0.005$ Pa·s, $\mu_m = 0.05$ Pa·s, for the typical condition. The densities and viscosities of each phase are assumed to be constant through the process. The continuity equation is as follows:

$$\nabla \cdot U = 0, \tag{3}$$

where U is the velocity of the fluid. The transport equations are as follows:

$$\begin{aligned} \frac{\partial \alpha_c}{\partial t} + \nabla \cdot (U \cdot \alpha_c) &= 0, \\ \frac{\partial \alpha_m}{\partial t} + \nabla \cdot (U \cdot \alpha_m) &= 0, \\ \frac{\partial \alpha_d}{\partial t} + \nabla \cdot (U \cdot \alpha_d) &= 0. \end{aligned} \tag{4}$$

And the momentum equation is given by

$$\frac{\partial U}{\partial t} + \nabla \cdot (UU) = -\frac{\nabla p}{\rho} + \nabla \cdot \frac{\mu}{\rho}\left[\nabla U + \nabla U^T\right] + f, \tag{5}$$

where p is the pressure and f is the source term calculated via the continuum surface force (CSF) approach [26–28]. And the interfacial tension coefficients of the inner interface σ_i and the outer interface σ_o are 0.001 N/m.

2.2. Numerical Solutions. The finite volume-based commercial software Fluent 6.3 is used to solve the governing equations. The computational domains of the curved minichannel presented in Figure 1 are discrete d by structured quadrilateral meshes. The finite volume method is used to solve the governing equations in this study. The discretization of the momentum equation is calculated by the second-order upwind scheme. Generally, the average Reynold number for the flows in the curved minichannel is less than 10, so that the flow can be treated as the laminar flow. The pressure and velocity coupling is achieved by using the Semi-Implicit Method for Pressure-Linked Equations (SIMPLE) algorithm. The interface is reconstructed following the second-order piecewise linear interface construction (PLIC) [29] method.

2.3. Grid Independence Test. To verify the grid independence, several different sizes of mesh are used. Figure 2 shows the compound droplet flowing in the curved minichannel at different mesh resolutions. As shown in the figure, there is a dispersion of inner droplet motion for cell number of 23604 and 73360. Nevertheless, the difference in simulation results between 73360 and 106970 cells is minor. Since the increase in the cell number induces greater computational cost, the cell number of 250399 is adopted for the current simulation.

2.4. Case Validation. To validate the theoretical model, the numerical simulation is compared with the experimental results. Figure 3 shows the schematic of the validation experiment setup, including syringe bumps, curved minichannel, high-speed camera, and computer. The water solutions with 5% wt. polyvinyl alcohol are used as inner phase and continuous phase. The benzene and dichloroethane solution with 7% wt. polystyrene is used as the middle phase. The high-speed camera (Photron, FASTCAM SA4) is used to capture the motion of the compound droplet. The syringe pumps (Longer, LSP01-1BH) are used to generate compound droplets with a microfluidic chip. The flow rates of the inner phase, middle phase, and continuous phase

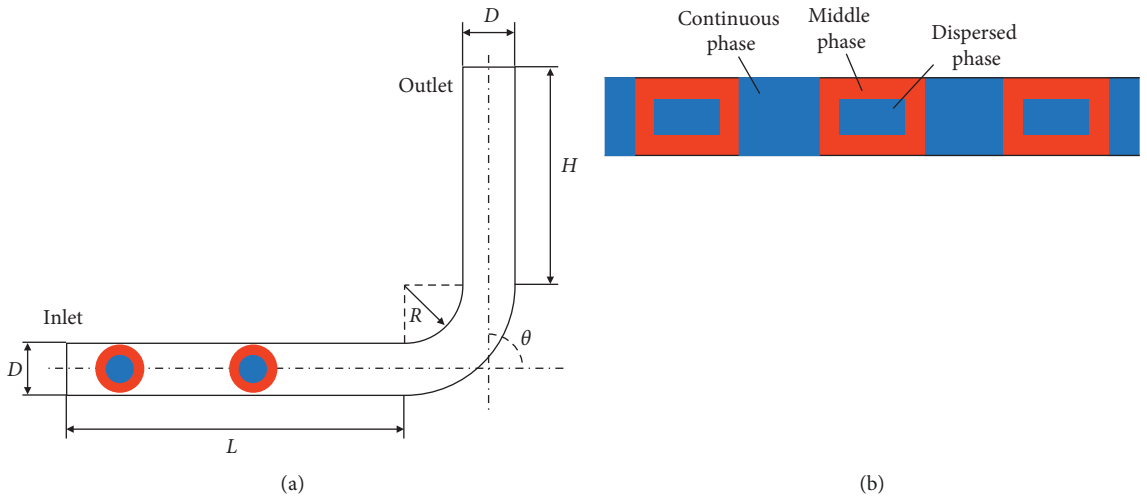

Figure 1: Schematics and computational domain of the mathematical model: (a) compound droplet deformation in the curved minichannel; (b) compound droplet formation.

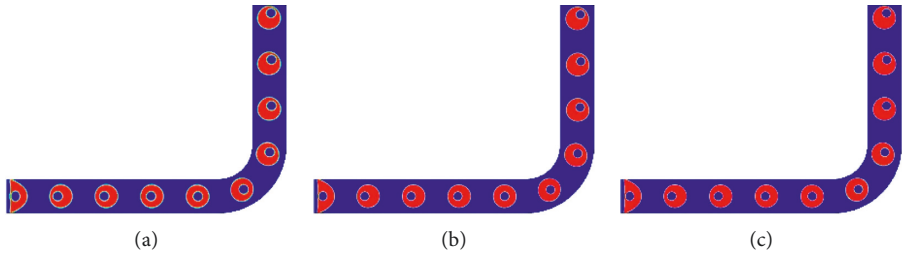

Figure 2: Grid independence test of different cell numbers n_c: (a) $n_c = 23604$; (b) $n_c = 73360$; (c) $n_c = 106970$.

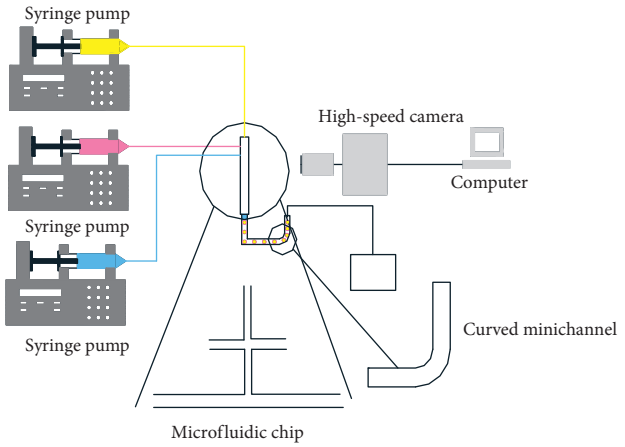

Figure 3: Schematic of the validation experiment setup.

are 5 ml/h, 5 ml/h, and 15 ml/h, respectively. Figure 4 compares the numerical simulation with the experimental results with different curved angles. The good agreements validate that the theoretical model is capable of predicting the hydrodynamic behavior of the compound droplet in the curved minichannel.

3. Results and Discussion

Based on the above model, the deformation behaviors of the compound droplets in the curved minichannel are predicted. The effects of curved angle, continuous phase, radius ratio, and viscosity of the middle phase are analyzed to reveal the deformation mechanism of the compound droplets in the curved minichannel.

3.1. The Deformation Behaviors of the Compound Droplet in the Curved Minichannel. Figure 5 illustrates the deformation process of the compound droplets in the curved minichannel, which can be divided into three stages, i.e., the initial stage, the turning stage, and the adjustment stage. During the initial stage, the compound droplet moves forward in the first straight section of the curved minichannel, driven by the syringe pump, shown in Figure 5(a). Figure 5(b) shows that the velocity at the center of the minichannel is the largest for the developed flow. Therefore, the inner droplet gradually moves towards the front of the compound droplet. During the turning stage, due to the centrifugal force at the curve, the velocity of the flow decreases and the pressure increases towards the center of the curve, resulting in the inner droplet moving radial direction. In the adjustment stage, the compound droplets move

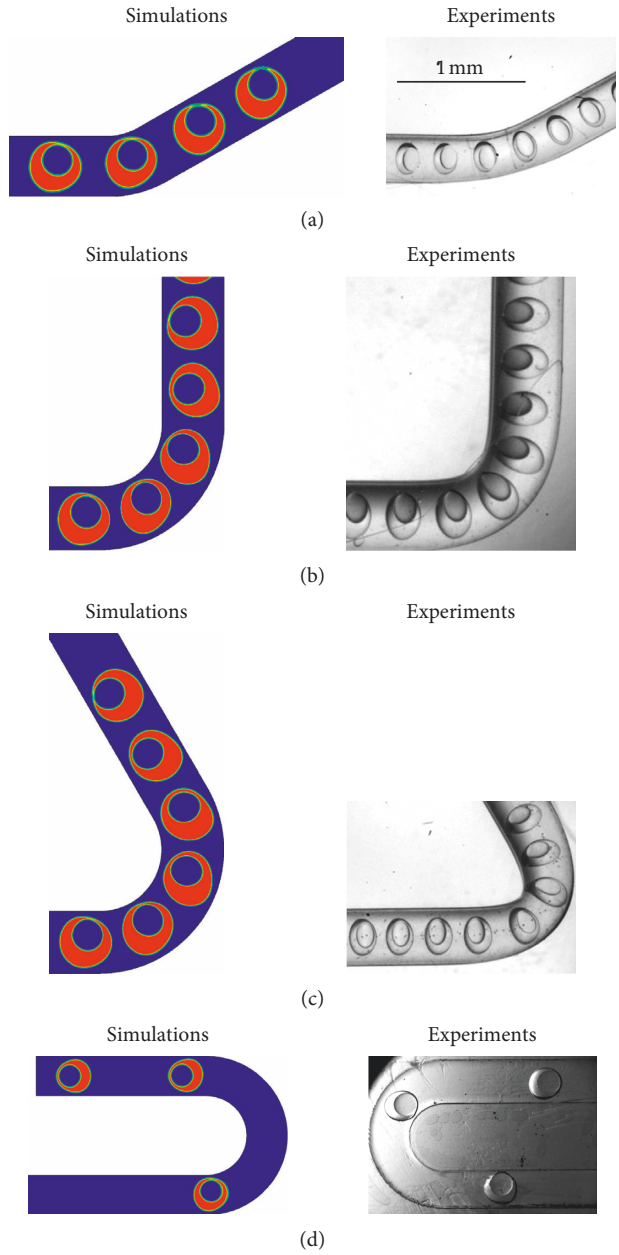

FIGURE 4: Comparison of the numerical simulation and the experimental results of compound droplet deformation in the curved minichannel: (a) $\theta = 30^{\circ}$; (b) $\theta = 90^{\circ}$; (c) $\theta = 120^{\circ}$; (d) $\theta = 180^{\circ}$.

forward in the second straight section of the curved minichannel. The compound droplet adjusts its shape to fit the developed channel flow. As shown in Figure 5(c), the increasing pressure gradient induced by the droplet deformation may lead to the breakup of the compound droplet.

3.2. Effect of the Curved Angle. There are diversities of the microfluidic device structures, especially the curved channels with different angles. Therefore, it is urgent to study the effect of the curved angle on the droplet deformation. Figure 6 shows the interface shape, pressure distribution, and velocity distribution of the curved minichannel with different curved angles. As the curved angle increases, there is more likely the breakup of the compound droplet. It mainly attributes to the increasing length of the curve, even though the radii of curvature and the centrifugal forces are the same. With the longer time at the turning, the pressure difference between inside and outside the compound droplet is larger, inducing a greater droplet deformation. As the inner droplet moves along the radial direction, there is less middle phase fluid near the wall between the dispersed phase and the continuous phase. Therefore, the eccentricity of the compound droplet is higher, and the breakup is easier to happen. According to the above simulation, large curved angle should be avoided in real applications.

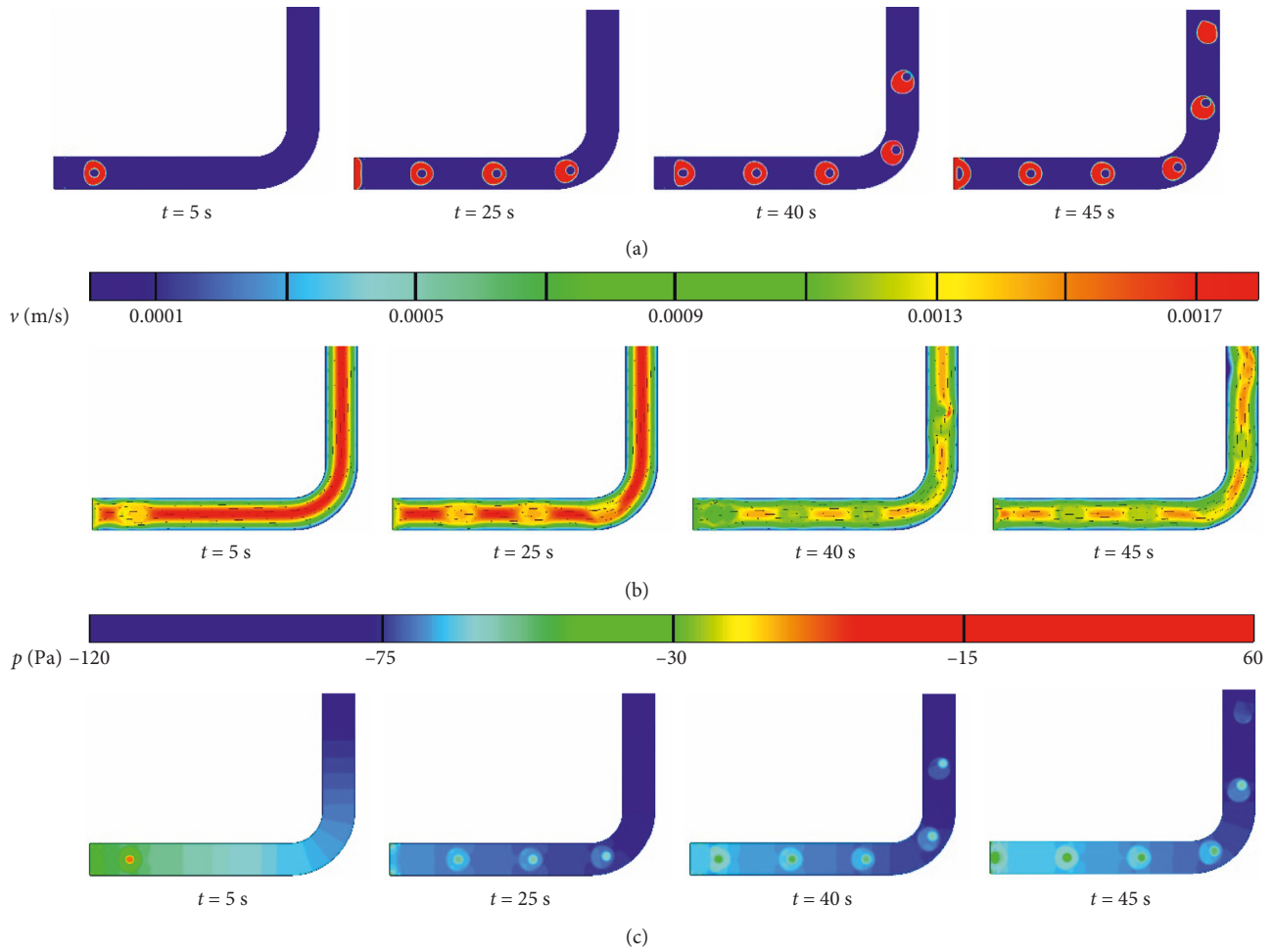

Figure 5: Time revolution of compound droplet deformation in the curved minichannel: (a) interface shape; (b) pressure distribution; (c) velocity distribution.

3.3. Effect of the Continuous Phase. The external fluid has a significant impact on the hydrodynamic behavior of the compound droplet. Hence, we introduce capillary number of the continuous phase Ca to generally analyze the effect of the continuous phase on the hydrodynamic behavior of the compound droplet:

$$\mathrm{Ca} = \frac{\mu_c u_c}{\sigma_o}, \tag{6}$$

where μ_c is the dynamic viscosity of the continuous phase and u_c is the average inlet velocity in the continuous phase.

As shown in Figure 7, with the increase of capillary number, the enhanced viscous effect of the continuous phase makes the compound droplet undergo a greater shear force from the continuous phase, resulting in the deformation of the compound droplet. The enhanced viscous also induces larger velocity gradient, so that the inner droplet moves far away from the center of the compound droplet, shown in Figure 8. Moreover, as shown in Figure 9, due to the weakened interfacial tension effect, the pressure in the middle phase is smaller, and the deformation of the compound droplet is hard to resist, especially parallel the direction of the minichannel. The presence of the inner droplet may lead to an oscillating deformation of the integral droplet. Therefore, with a relatively large capillary number, the concentricity of the compound droplet is larger, and the thickness of the middle phase near the wall is smaller, eventually leading to the breakup of the compound droplet.

3.4. Effect of Radius Ratio between Inner and Integral Droplets. The radius ratio between inner and integral droplets k is a critical factor to the deformation of the compound droplet, as the deformation of the integral droplet is affected by the deformation of the inner droplet. Figure 10 compares the deformation of the compound droplet with different radius ratios. At a low radius ratio, the motion and deformation of the inner droplet promote the deformation of the integral droplet. As the radius ratio grows, the high-pressure region in the inner droplet becomes closer to the outer interface. Consequently, the pressure gradient near the outer interface becomes larger, leading to a smaller curvature of the interface. Especially at a high radius ratio, the deformation of the integral droplet is suppressed by the inner droplet.

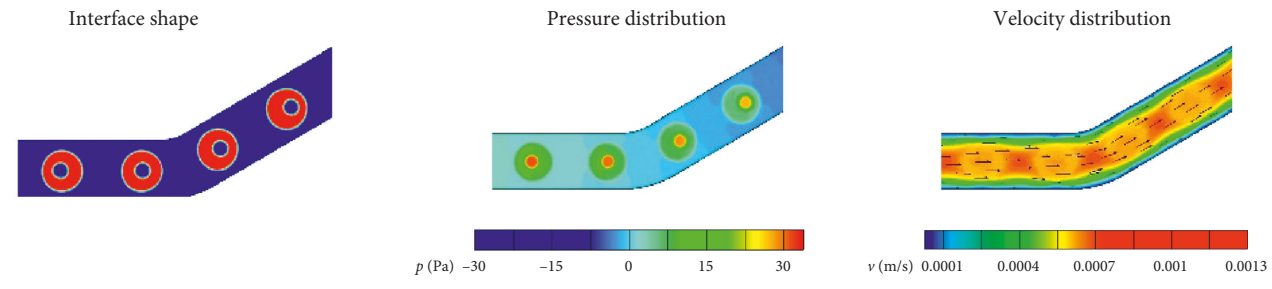

(a)

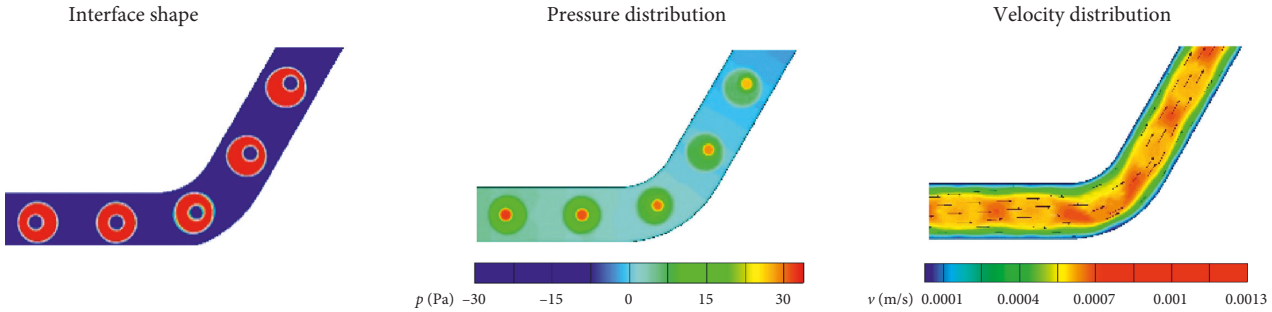

(b)

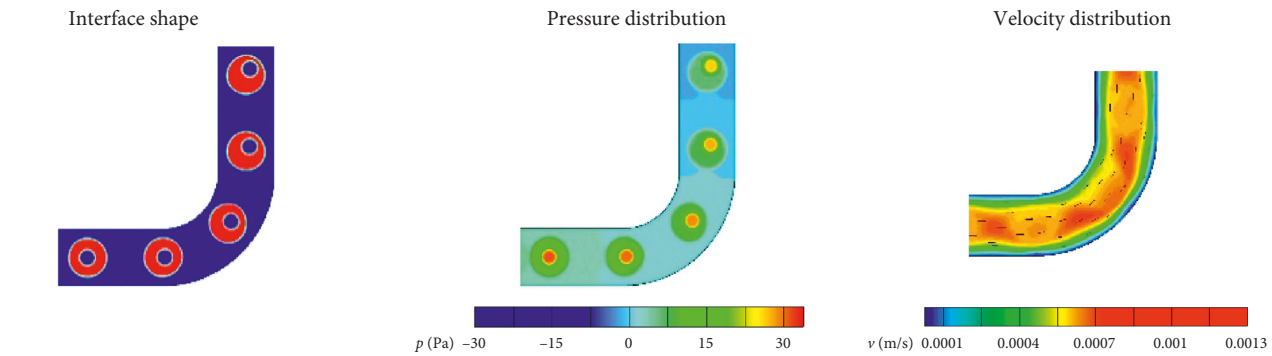

(c)

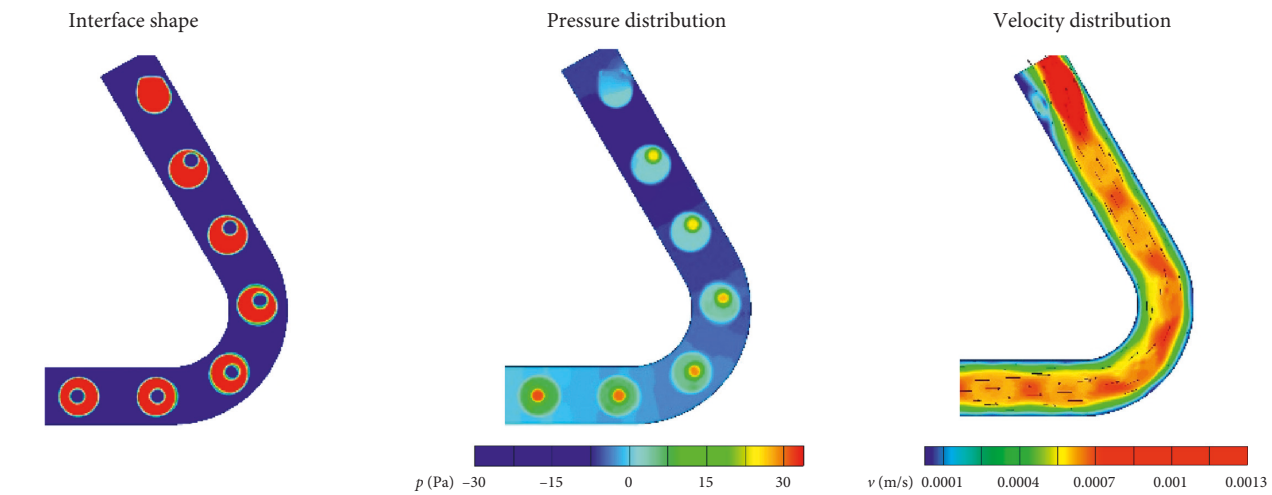

(d)

Figure 6: Continued.

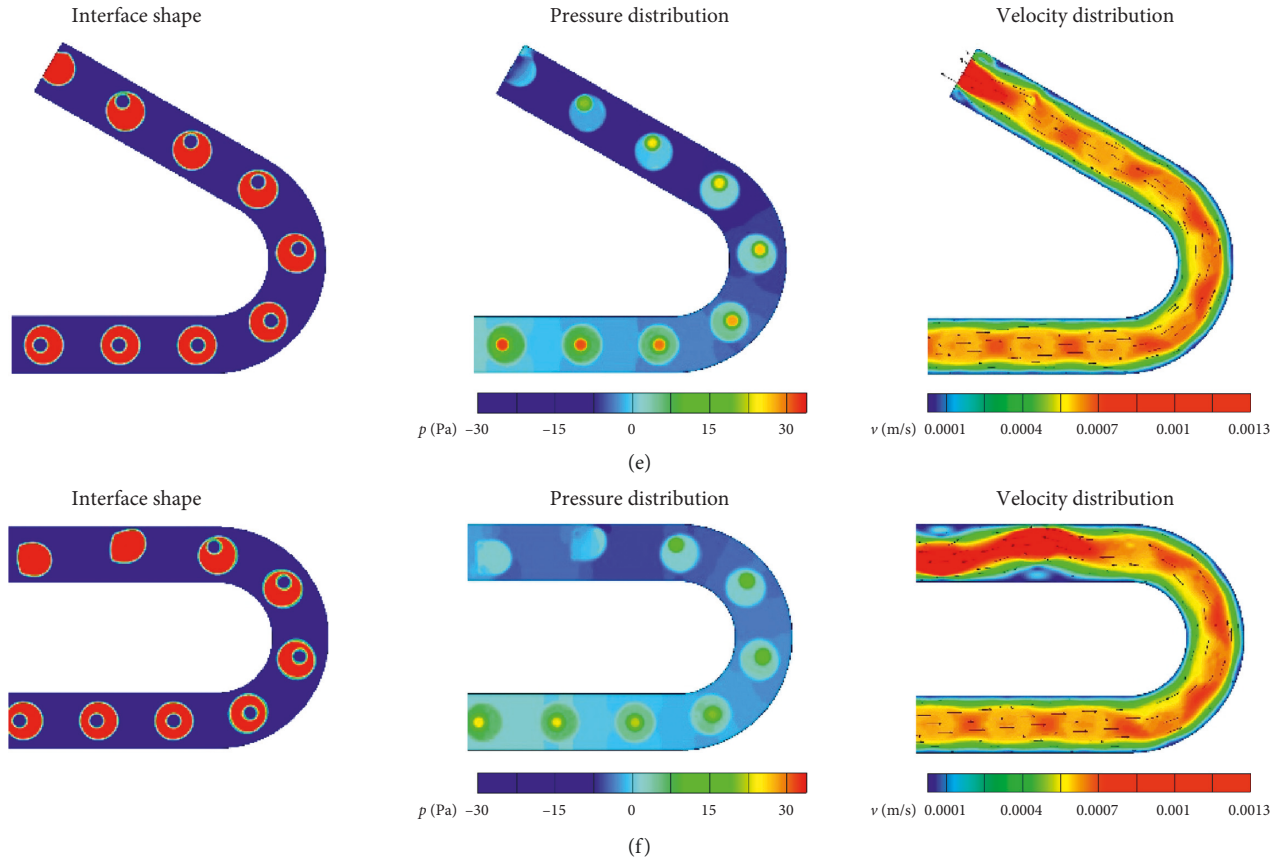

Figure 6: Effect of curved angle on the compound droplet deformation: (a) $\theta = 30^{\circ}$; (b) $\theta = 60^{\circ}$; (c) $\theta = 90^{\circ}$; (d) $\theta = 120^{\circ}$; (e) $\theta = 150^{\circ}$; (f) $\theta = 180^{\circ}$.

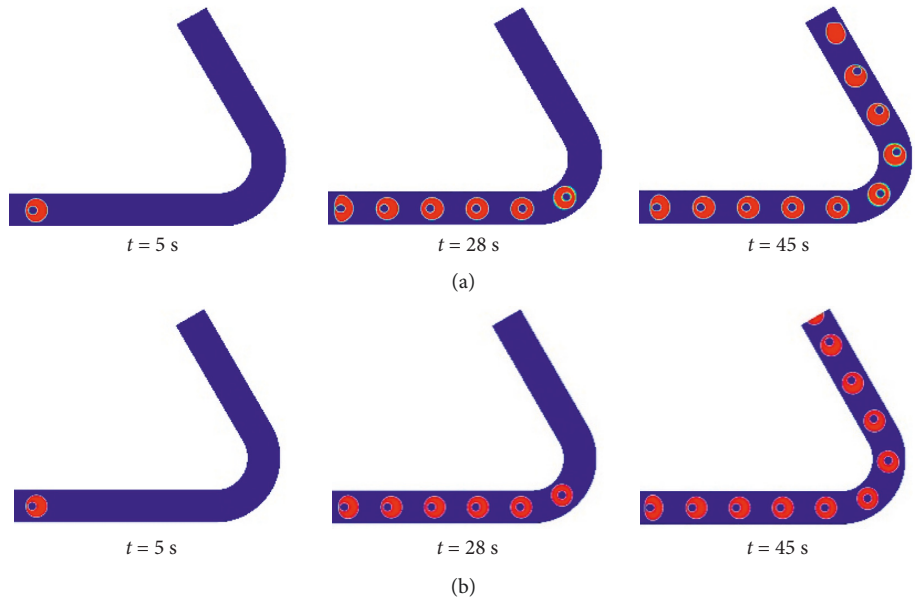

Figure 7: Effect of capillary number of continuous phase on the interface shape during compound droplet deformation: (a) Ca = 0.05; (b) Ca = 0.025.

3.5. Effect of the Viscosity of the Middle Phase. Figure 11 shows the effect of viscosity of the middle phase on the compound droplet deformation. As the viscosity of the middle phase increases, the increasing inertial effect suppresses the deformation of the compound droplet. Moreover, the motion of the inner droplet undergoes more

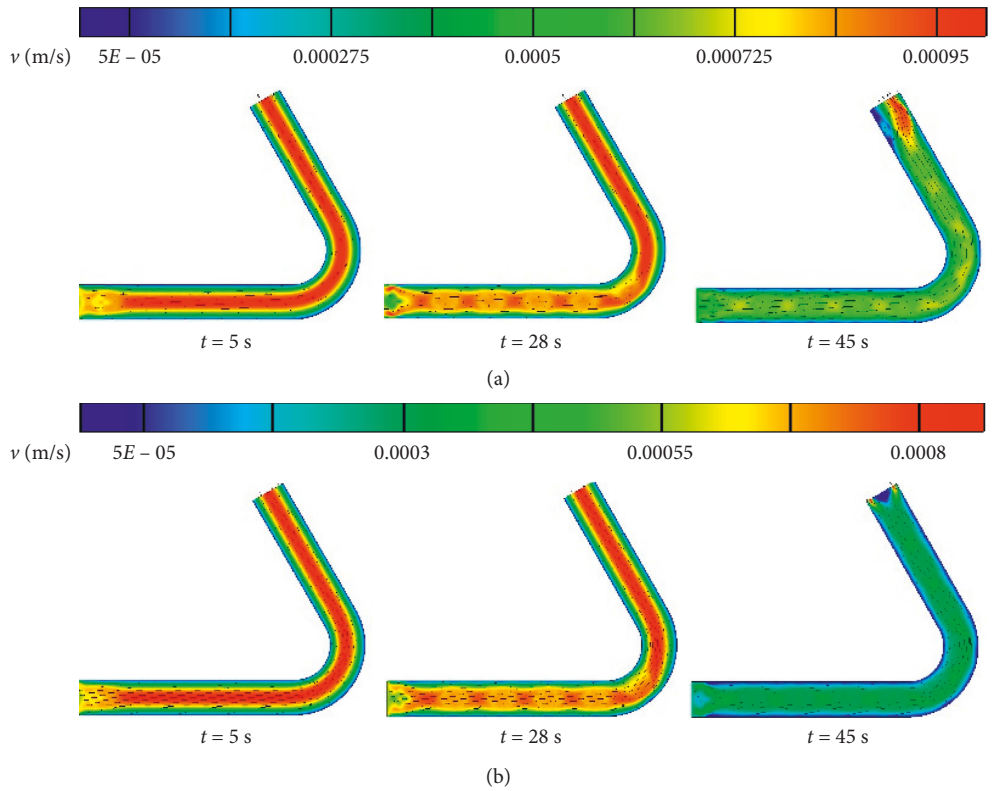

Figure 8: Effect of capillary number on the velocity distribution during compound droplet deformation: (a) Ca = 0.05; (b) Ca = 0.025.

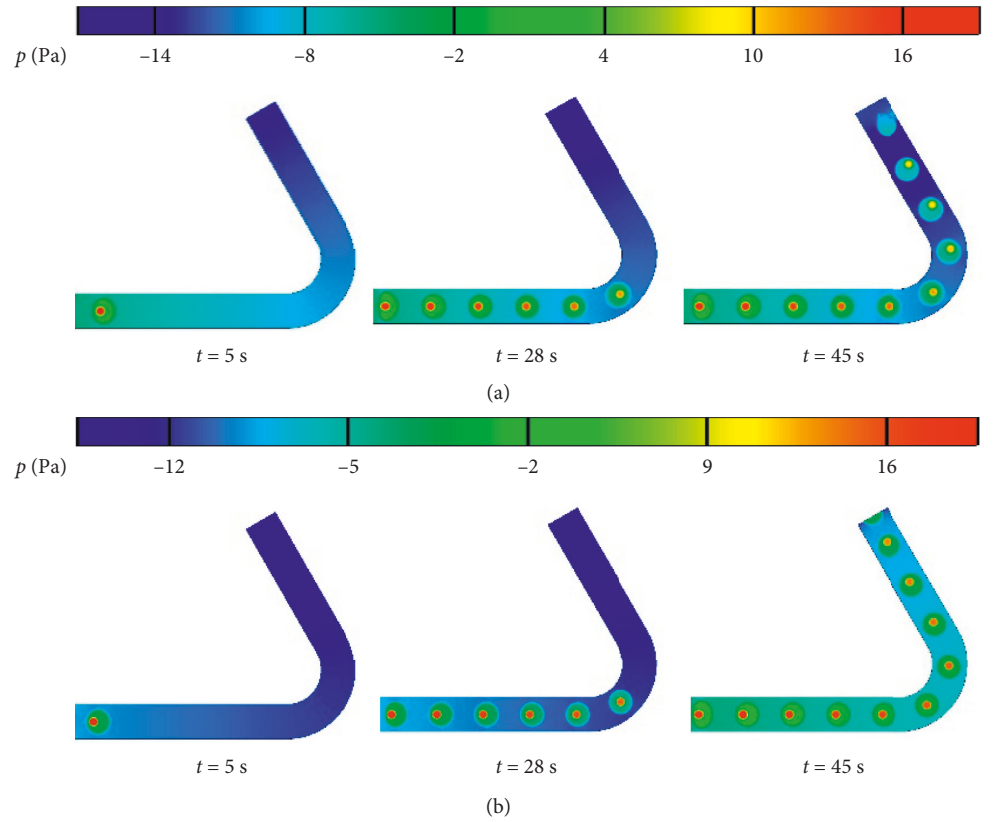

Figure 9: Effect of capillary number on the pressure distribution during compound droplet deformation: (a) Ca = 0.05; (b) Ca = 0.025.

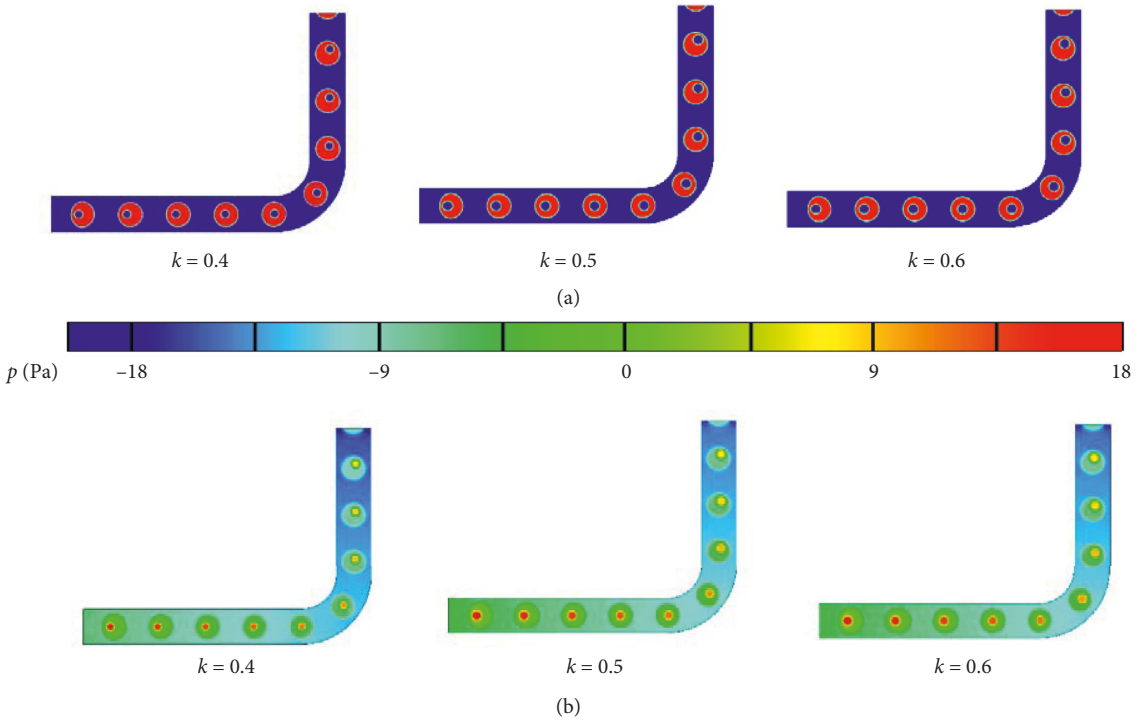

Figure 10: Effect of radius ratio on the compound droplet deformation: (a) interface shape; (b) pressure distribution.

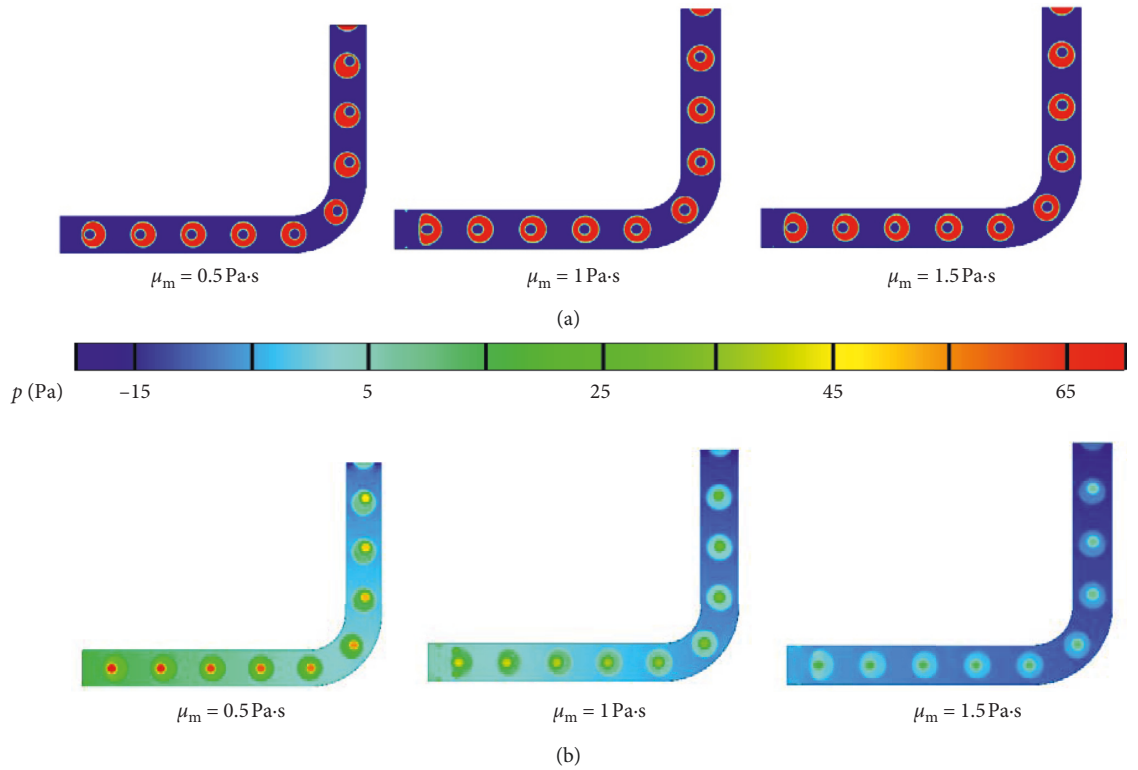

Figure 11: Effect of the viscosity of the middle phase on the compound droplet deformation: (a) interface shape; (b) pressure distribution.

resistance, resulting in the low concentricity of the compound droplet. As shown in Figure 11(b), the pressure difference across the outer interface is larger with high viscosity of the middle phase, indicating that the deformation of the compound droplet is larger.

4. Conclusions

Based on the VOF method, a theoretical model of the deformation behaviors of the compound droplets in the curved minichannel is developed to investigate the hydrodynamics of the compound droplets in the curved minichannel. The effects of curved angle, continuous phase, radius ratio, and viscosity of the middle phase are analyzed to reveal the deformation mechanism of the compound droplets in the curved minichannel. The results indicate that

(1) The motion of the compound droplets in the curved minichannel can be divided into three stages, i.e., the initial stage, the turning stage, and the adjustment stage.

(2) As the curved angle increases, the eccentricity of the compound droplet is higher and the breakup is easier to occur, due to the higher shear force.

(3) With a relatively large capillary number, the compound droplet exhibits greater deformation due to the increasing shear force from the continuous phase, eventually leading to the breakup of the compound droplet.

(4) At a low radius ratio, the deformation of the integral droplet is promoted by the motion and deformation of the inner droplet. However, at a high radius ratio, the deformation of the integral droplet is suppressed by the inner droplet.

This simulation not only provides a deep understanding of hydrodynamic behaviors of the compound droplet flowing in the curved minichannels but also contributes to precisely controlling the concentricity and sphericity of the compound droplet, which is of significance for the application of the microspheres. Three-dimensional simulation with a more complex channel structure may be considered in the future research work.

Nomenclature

Ca: Capillary number
k: Radius ratio between the inner and integral droplets
n_c: Cell numbers
p: Pressure (Pa)
t: Time (s)
U: Velocity of the fluid (m/s)

Greek symbols
θ: Curved angle (°)
α: Volume fraction
μ: Dynamic viscosity (Pa·s)
ρ: Density (kg m^{-3})
σ: Surface tension (N/m)

Subscripts
c: Continuous phase
m: Middle phase
d: Dispersed phase
i: Inner interface
o: Outer interface.

Data Availability

The data used to support the findings of this study are included within the article.

Conflicts of Interest

The authors declare that there are no conflicts of interest regarding the publication of this paper.

Acknowledgments

This work was supported by the National Natural Science Foundation of China (no. 51776037).

References

[1] C. Zhang, F. Yu, X. Li, and Y. Chen, "Gravity–capillary evaporation regimes in microgrooves," *AIChE Journal*, vol. 65, no. 3, pp. 1119–1125, 2019.

[2] H. Song, D. L. Chen, and R. F. Ismagilov, "Reactions in droplets in microfluidic channels," *Angewandte Chemie International Edition*, vol. 45, no. 44, pp. 7336–7356, 2006.

[3] B. Hadwen, G. Broder, D. Morganti et al., "Programmable large area digital microfluidic array with integrated droplet sensing for bioassays," *Lab on a Chip*, vol. 12, no. 18, pp. 3305–3313, 2012.

[4] Y. Gao, C. U. Chan, Q. Gu et al., "Controlled nanoparticle release from stable magnetic microbubble oscillations," *NPG Asia Materials*, vol. 8, no. 4, p. e260, 2016.

[5] J. Wang, L. Sun, M. Zou et al., "Bioinspired shape-memory graphene film with tunable wettability," *Science Advances*, vol. 3, no. 6, Article ID e1700004, 2017.

[6] V. V. Tyagi, S. C. Kaushik, S. K. Tyagi, and T. Akiyama, "Development of phase change materials based microencapsulated technology for buildings: a review," *Renewable and Sustainable Energy Reviews*, vol. 15, no. 2, pp. 1373–1391, 2011.

[7] C. Zhang, Y. Chen, R. Wu, and M. Shi, "Flow boiling in constructal tree-shaped minichannel network," *International Journal of Heat and Mass Transfer*, vol. 54, no. 1–3, pp. 202–209, 2011.

[8] K. Du, M. Liu, T. Wang et al., "Recent progress in icf target fabrication at RCLF," *Matter and Radiation at Extremes*, vol. 3, no. 3, pp. 135–144, 2018.

[9] E. M. Campbell, V. N. Goncharov, T. C. Sangster et al., "Laser-direct-drive program: promise, challenge, and path forward," *Matter and Radiation at Extremes*, vol. 2, no. 2, pp. 37–54, 2017.

[10] K. Lan, J. Liu, Z. Li et al., "Progress in octahedral spherical hohlraum study," *Matter and Radiation at Extremes*, vol. 1, no. 1, pp. 8–27, 2016.

[11] V. Hessel, H. Löwe, and F. Schönfeld, "Micromixers—a review on passive and active mixing principles," *Chemical Engineering Science*, vol. 60, no. 8, pp. 2479–2501, 2005.

[12] F. Sarrazin, L. Prat, N. Di Miceli, G. Cristobal, D. R. Link, and D. A. Weitz, "Mixing characterization inside microdroplets engineered on a microcoalescer," *Chemical Engineering Science*, vol. 62, no. 4, pp. 1042–1048, 2007.

[13] L. Kong, X. Gao, R. Li, and J. Han, "Bubbles in curved tube flows—an experimental study," *International Journal of Heat and Mass Transfer*, vol. 105, pp. 180–188, 2017.

[14] X. Liu, Y. Chen, and M. Shi, "Dynamic performance analysis on start-up of closed-loop pulsating heat pipes (clphps)," *International Journal of Thermal Sciences*, vol. 65, pp. 224–233, 2013.

[15] Z. Che, T. N. Wong, and N.-T. Nguyen, "An analytical model for a liquid plug moving in curved microchannels," *International Journal of Heat and Mass Transfer*, vol. 53, no. 9-10, pp. 1977–1985, 2010.

[16] Z. Che, N.-T. Nguyen, and T. N. Wong, "Analysis of chaotic mixing in plugs moving in meandering microchannels," *Physical Review E*, vol. 84, no. 6, Article ID 066309, 2011.

[17] W. A. H. S. S. Wewala, J. K. Kasi, A. K. Kasi, and N. Afzulpurkar, "Design, simulation and comparison of ascending and descending curvilinear microchannels for cancer cell separation from blood," *Biomedical Engineering: Applications, Basis and Communications*, vol. 25, no. 3, Article ID 1350037, 2013.

[18] J. Wang, J. Wang, L. Feng, and T. Lin, "Fluid mixing in droplet-based microfluidics with a serpentine microchannel," *RSC Advances*, vol. 5, no. 126, pp. 104138–104144, 2015.

[19] L. Jiang, Y. Zeng, H. Zhou, J. Y. Qu, and S. Yao, "Visualizing millisecond chaotic mixing dynamics in microdroplets: a direct comparison of experiment and simulation," *Biomicrofluidics*, vol. 6, no. 1, Article ID 012810, 2012.

[20] Z. Y. Luo and B. F. Bai, "Dynamics of capsules enclosing viscoelastic fluid in simple shear flow," *Journal of Fluid Mechanics*, vol. 840, pp. 656–687, 2018.

[21] Y. Chen, X. Liu, and M. Shi, "Hydrodynamics of double emulsion droplet in shear flow," *Applied Physics Letters*, vol. 102, no. 5, Article ID 051609, 2013.

[22] Y. Chen, X. Liu, C. Zhang, and Y. Zhao, "Enhancing and suppressing effects of an inner droplet on deformation of a double emulsion droplet under shear," *Lab on a Chip*, vol. 15, no. 5, pp. 1255–1261, 2015.

[23] C. W. Hirt and B. D. Nichols, "Volume of fluid (VOF) method for the dynamics of free boundaries," *Journal of Computational Physics*, vol. 39, no. 1, pp. 201–225, 1981.

[24] C. W. Hirt, J. E. Richardson, and K. S. Chen, "Simulation of transient and three-dimensional coating flows using a volume-of-fluid technique," in *Proceedings of the 50th Annual Conference of the Society for Imaging and Science Technology*, Springfield: Society for Imaging Science and Technology, Boston, MA, USA, May 1997.

[25] J. Li, Y. Y. Renardy, and M. Renardy, "Numerical simulation of breakup of a viscous drop in simple shear flow through a volume-of-fluid method," *Physics of Fluids*, vol. 12, no. 2, pp. 269–282, 2000.

[26] J. U. Brackbill, D. B. Kothe, and C. Zemach, "A continuum method for modeling surface tension," *Journal of Computational Physics*, vol. 100, no. 2, pp. 335–354, 1992.

[27] Y. Chen, C. Zhang, M. Shi, and Y. Yang, "Thermal and hydrodynamic characteristics of constructal tree-shaped minichannel heat sink," *AIChE Journal*, vol. 56, no. 8, pp. 2018–2029, 2010.

[28] K. Yokoi, "A density-scaled continuum surface force model within a balanced force formulation," *Journal of Computational Physics*, vol. 278, pp. 221–228, 2014.

[29] D. Gueyffier, J. Li, A. Nadim, R. Scardovelli, and S. Zaleski, "Volume-of-fluid interface tracking with smoothed surface stress methods for three-dimensional flows," *Journal of Computational Physics*, vol. 152, no. 2, pp. 423–456, 1999.